water

MDPI

Article

Numerical Investigation of the Hydrodynamic Performance of a V-Type Wave Dissipation System and Amphibious Landing Equipment Under Different Combined Fields

Junming Hu [1], Chengshuai Song [1], Jiaxian Deng [2,*], Xueying Yu [1] and Daiyu Zhang [1]

[1] School of Naval Architecture and Ocean Engineering, Jiangsu University of Science and Technology, Zhenjiang 212100, China; junming5779@126.com (J.H.); song681505@163.com (C.S.); yuxueying@just.edu.cn (X.Y.); daiyu.zhang@outlook.com (D.Z.)
[2] Shanghai Salvage, Ministry of Transport, Shanghai 200082, China
* Correspondence: 15061390796@163.com

Abstract

This study analyzes the hydrodynamic performance of a V-type wave dissipation system and amphibious landing equipment under different combined fields using the Reynolds-averaged Navier–Stokes (RANS) method. A three-dimensional numerical wave tank is established to simulate regular waves and validate the performance of an airbag-type floating breakwater. This study evaluates the optimal hydrodynamic performance of a V-type wave dissipation system under various configurations in a wave-only field and subsequently compares the efficacy of the better-performing system across multiple environmental conditions. The results show that the V-type wave dissipation system in the configurations of 30° and 45° angles is more favorable for the flow field and the amphibious landing equipment behind it. Compared to the wave-only condition, the time histories of wave heights under both wave-current and wind-wave conditions present an obvious phase advancement. In the wave-current field, a following current reduces the wave height and shortens the wave period. Conversely, in the wind-wave field, a following wind velocity leads to a certain increase in wave height while exerting minimal impact on the wave period. Compared to the wave-only condition, the peak and trough values of the wave height monitoring points in the combined wind-wave-current field show an increasing trend, with a significant increase in resistance and a shorter resistance period for the amphibious landing equipment behind the V-type wave dissipation system. This study shows that the selected V-type wave dissipation system proves to be more effective in wave-only and wave-current conditions, providing valuable references for the engineering application of this system.

Keywords: numerical wave tank; V-type wave dissipation system; amphibious landing equipment; different combined fields; hydrodynamic performance

Check for updates

Academic Editor: Chin H Wu

Received: 30 December 2025
Revised: 23 January 2026
Accepted: 23 January 2026
Published: 25 January 2026

Copyright: © 2026 by the authors. Licensee MDPI, Basel, Switzerland. This article is an open access article distributed under the terms and conditions of the Creative Commons Attribution (CC BY) license.

1. Introduction

The marine environment is complex and changeable. When a ship releases amphibious equipment through the stern hatch in high sea conditions, it is difficult to ensure safety and efficiency due to the influence of harsh maritime environmental factors such as waves. To improve the safety of releasing equipment, it is necessary to deploy a wave dissipation system near the stern of the ship to reduce the sea condition level in the critical stern area, improve the flow field around the stern, and enhance the ship's adaptability to high-sea

conditions and its operational capability under complex marine environments. Therefore, accurately assessing and studying the wave dissipation system's shielding characteristics for amphibious landing equipment is of significant importance.

Based on research on wave-related theories, it has been found that in water body motion, the wave energy is mostly concentrated in the surface layer, with 90–98% of the total wave energy concentrated within 2–3 times the wave height range of the surface layer [1]. Currently, research on wave dissipation facilities mainly focuses on bottom-mounted breakwaters and floating breakwaters. Bottom-mounted breakwaters are generally constructed in coastal areas near piers and ports, where foundation conditions and water depth requirements are high. These structures have a significant environmental impact and require substantial financial and material resources. Furthermore, they use more materials in the lower part of the water body, where energy is low, and fewer materials in the upper part of the water body, where energy is high, making the material usage inconsistent with wave energy distribution [2]. Compared to traditional bottom-mounted breakwaters, floating breakwaters float on the sea surface, providing better interaction with seawater, with less influence from water depth and marine conditions. They also have good environmental performance, experience minimal impacts from tidal variations, lower construction costs, and strong adaptability to foundations, making them widely used in marine engineering.

The excellent wave dissipation performance is an important indicator for evaluating the shielding characteristics of the wave dissipation system for amphibious landing equipment. The layout, structural type, and material properties of floating breakwaters all significantly affect wave dissipation performance. Currently, the research on wave dissipation systems mainly employs model testing and numerical simulation methods. Theoretical studies are limited by the constraints of potential flow theory and cannot account for viscous effects. Additionally, the nonlinear and complex flow field caused by the interaction between structures under high-sea conditions further limits theoretical research. Model testing methods are accurate and reliable, but costly [3–5]. Eva Loukogeorgaki et al. [6] (2014) evaluated the structural response and hydrodynamic performance of a floating breakwater based on model tests. The results indicate that the structural response of the floating breakwater is strongly dependent on wave period, while wave height and incident wave angle mainly influence the structural response in the low-frequency range. Under oblique wave conditions, its functional efficiency and structural integrity perform relatively well. He et al. [7] (2023) conducted a series of experimental studies on the hydrodynamic characteristics of a floating breakwater with vertical plates as wave-absorption components under regular waves. The effects of installation position, number of plate rows, plate porosity, and plate extension height on its wave-absorption performance and motion response were investigated. The research shows that the primary working mechanism of vertical plates as wave-absorption components lies in water confinement. The water confined by the plates significantly alters the dynamic characteristics of the floating breakwater and shifts the natural period of pitch motion toward longer waves. Wang et al. [8] proposed a curved-plate breakwater structure consisting of multiple curved plates suspended from supporting piles. Two-dimensional physical model tests under regular waves were conducted to study the wave-absorption performance of this breakwater. The results demonstrate that the performance of the curved-plate breakwater is superior to that of horizontal-plate breakwaters. When the relative width is approximately 0.2, the transmission coefficient can be reduced to 0.5. The performance of the breakwater is related to relative submergence depth, relative height, and relative gap, while the number of curved plates has little influence on wave-absorption performance. With the development of Computational Fluid Dynamics (CFD), numerical calculations that handle viscous flow fields have overcome the limitations of theoretical methods, providing good economic benefits. The numeri-

cal results are consistent with experimental results and have become an important tool for studying the hydrodynamic characteristics of wave dissipation systems in numerical wave tanks [9].

Research on numerical wave tank wave dissipation systems is based on a three-dimensional numerical wave tank. Domestic and international scholars have conducted extensive research on numerical wave tanks, making significant progress in this area [10–14]. Regarding wave dissipation systems within numerical wave tanks, researchers worldwide have also carried out a series of investigations. Zhang et al. [15] (2018) simulated the viscous flow of wave–structure interaction for rectangular and inverted-type floating breakwaters and designed an L-shaped floating breakwater. Sensitivity analysis of the main structural dimensions for wave protection performance showed that, under the condition of the same wave barrier length, the L-shaped floating breakwater exhibited superior overall performance compared to rectangular and inverted-type ones. Christensen et al. [16] (2018) attached wing plates and porous media to the sides of floating breakwaters to create a new type of floating breakwater and conducted numerical and experimental studies on the influence of two different damping mechanisms. Li et al. [17] (2020) established a numerical model considering the nonlinear interaction between waves and arc plate breakwaters using wave-velocity method, volume of fluid (VOF) method, and finite volume method. Their study, combined with experiments, analyzed the factors affecting the wave dissipation performance of arc plate breakwaters. The results indicate that when the relative width of the plate is greater than 0.22, the transmission coefficient can be maintained below 0.5. Abdullah et al. [18] (2020) employed a genetic algorithm to analyze the optimal hydrodynamic performance of a double-row floating breakwater, revealing that the transmission coefficient could be reduced to 0.3. Zhang and Magee [19] (2021) conducted a comparative analysis of the protective efficacy between floating breakwaters with different pontoon-frame configurations and conventional single floating breakwaters. The results indicate that the L-shaped floating breakwater significantly reduces wave transmission in the absence of floating tanks, while the pontoon-frame configuration demonstrates the most pronounced motion suppression effect on the floating tanks. Ran et al. [20] (2021) combined numerical simulation and model testing to study the wave dissipation characteristics of V-shaped flexible floating breakwaters. They conducted numerical analysis of the wave dissipation characteristics of flexible floating breakwaters under different layouts using AQWA 2021 R1 software. Sun et al. [21] (2022) used fluid–structure interaction (FSI) methods to numerically simulate the box-type floating breakwater under wave action. Based on model validation, the study focused on investigating the wave dissipation mechanism of box-type floating breakwaters. Yuan Pei yin [22] (2023) used viscous flow CFD methods to establish a numerical wave tank and studied the wave climbing characteristics of box-type and sloping floating breakwaters. The analysis showed that, compared to box-type breakwaters, sloping breakwaters had a smoother wave climbing height variation and better wave overtopping prevention. Ji et al. [23] (2023) used both numerical and experimental methods to study the hydrodynamic performance of different types of floating breakwaters, finding that a double-hull floating breakwater with wave nets and wave balls had superior wave dissipation performance.

Computational research on such wave dissipation systems involves viscous flow around structures, where the interaction between structures and the flow field is complex. The mechanism of action is intricate, and factors such as layout, structural type, and flow patterns all influence the wave dissipation performance of the system. Current research remains insufficiently comprehensive and in-depth, with most studies focusing on the wave dissipation system itself (shape, configuration, arrangement). For multi-body coupled motions, especially those involving wave dissipation systems with ships or amphibious

landing equipment, the interplay among the structures and between the structures and the flow field is not yet fully understood due to the complexity of the flow and the nonlinearity of the motions. Existing research has largely concentrated on model testing methods [24–27]. Therefore, there is an urgent need for research focused on the hydrodynamic interactions between wave dissipation systems and ships or amphibious landing equipment.

To enhance the sea-keeping capability of ships and their operational effectiveness in complex marine environments, as well as to improve the safety of deployed equipment, this paper conducted a computational study on the influence of wave-absorption systems on the hydrodynamic characteristics of amphibious landing equipment using CFD methods. A wind-wave-current environment was numerically constructed. The study aimed to evaluate the hydrodynamic performance of the V-type wave-absorption system and amphibious landing equipment, reveal the working mechanisms of the wave-absorption system, and provide valuable references for the engineering design and application of wave-absorption systems.

2. Fundamental Numerical Theory

2.1. RANS Equations

The hydrodynamic performance of the V-type wave dissipation system is solved based on the viscous flow theory using the Navier–Stokes (N-S) equations, considering the nonlinearity of the flow field and the incompressibility of the fluid. The continuity equation and Reynolds-averaged N-S equations for the fluid are as follows [28,29]:

$$\frac{\partial \overline{u_i}}{\partial x_i} = 0 \tag{1}$$

$$\frac{\partial \overline{u_i}}{\partial t} + \overline{u_j}\frac{\partial \overline{u_i}}{\partial x_j} + \frac{\partial \overline{u'_i u'_j}}{\partial x_j} = -\frac{1}{\rho}\frac{\partial \overline{p}}{\partial x_i} + \nu\frac{\partial^2 \overline{u_i}}{\partial x_j \partial x_j} + f_i \tag{2}$$

In the equations, ρ denotes the fluid density, t represents time, and u_i and u'_i correspond to the time-averaged flow velocity and instantaneous fluctuating flow velocity, respectively. Furthermore, p signifies the static pressure, ν is the kinematic viscosity, and f_i represents the body force per unit mass. For incompressible viscous fluid motion, the time-averaged continuity equation and Reynolds-averaged N-S equations together form the governing system of equations. Compared to the N-S equations, the Reynolds-averaged N-S equations include the Reynolds stress term $\partial \overline{u'_i u'_j}/\partial x_j$, which introduces an additional unknown quantity into the equations. The number of unknowns in the governing system exceeds the number of equations, causing the system to be unclosed and difficult to solve. Therefore, it is necessary to make an assumption about the Reynolds stress term $\partial \overline{u'_i u'_j}/\partial x_j$ and close the system by constructing the SST $k-\omega$ turbulence model, which links the time-averaged and fluctuating values, thus making the governing system closed and solvable.

2.2. Turbulence Model

The SST $k-\omega$ turbulence model was applied to study the V-type numerical wave tank wave dissipation system. The SST $k-\omega$ turbulence model is a hybrid model that combines the advantages of the Standard $k-\varepsilon$ turbulence model for far-field calculations and the benefits of the Standard $k-\omega$ turbulence model for near-wall calculations. The SST $k-\omega$ turbulence model equation accounts for the transport characteristics of turbulent shear stress, making it theoretically more advanced and complete than the Standard $k-\omega$ turbulence model. It can accurately predict complex turbulent flows with separation. Additionally, it considers transport effects in the turbulent viscosity, inheriting the advantages

of the Standard $k-\varepsilon$ turbulence model for far-field calculations, offering higher applicability and reliability. The transport equations for turbulent kinetic energy k and turbulent dissipation ω are expressed as follows [30–32]:

$$\frac{\partial}{\partial t}(\rho k)+\frac{\partial}{\partial x_j}(\rho k\overline{u_j})=\frac{\partial}{\partial x_j}\left[(\mu+\sigma_k\mu_t)\frac{\partial k}{\partial x_j}\right]+P_k-\rho\beta^*k\omega \tag{3}$$

$$\begin{aligned}\frac{\partial}{\partial t}(\rho\omega)+\frac{\partial}{\partial x_j}(\rho\omega\overline{u_j})=\frac{\partial}{\partial x_j}\left[(\mu+\sigma_\omega\mu_t)\frac{\partial\omega}{\partial x_j}\right]+\\ \rho\alpha S^2-\rho\beta\omega^2+2\rho(1-F_1)\sigma_{\omega2}\frac{1}{\omega}\frac{\partial k}{\partial x_j}\frac{\partial\omega}{\partial x_j}\end{aligned} \tag{4}$$

The formulas for the turbulent kinetic energy generation terms P_k, turbulent viscosity coefficient μ_t, and parameters σ_k and σ_ω in Equations (3) and (4) are as follows:

$$P_k=\min\left[\mu_t\frac{\partial\overline{u_i}}{\partial x_j}\left(\frac{\partial\overline{u_i}}{\partial x_j}+\frac{\partial\overline{u_j}}{\partial x_i}\right),10\cdot\beta^*\rho k\omega\right] \tag{5}$$

$$\mu_t=\frac{\rho\alpha_1k}{\max(\alpha_1\omega,\Omega F_2)} \tag{6}$$

$$\sigma_k=\frac{1}{F_1/\sigma_{k1}+(1-F_1)/\sigma_{k2}} \tag{7}$$

$$\sigma_\omega=\frac{1}{F_1/\sigma_{\omega1}+(1-F_1)/\sigma_{\omega2}} \tag{8}$$

The terms F_1 and F_2 in Equations (5)–(8) are blending functions, which are defined as follows:

$$F_1=\tanh(\Phi_1^4) \tag{9}$$

$$\Phi_1=\min\left[\max\left(\frac{\sqrt{k}}{\beta^*\omega y},\frac{500v}{y^2\omega}\right),\frac{4\rho\sigma_{\omega2}k}{CD_{k\omega}y^2}\right] \tag{10}$$

$$CD_{k\omega}=\max\left[2\rho\sigma_{\omega2}\frac{1}{\omega}\frac{\partial k}{\partial x_j}\frac{\partial\omega}{\partial x_j},10^{-10}\right] \tag{11}$$

$$F_2=\tanh(\Phi_2^2) \tag{12}$$

$$\Phi_2=\max\left[\frac{2\sqrt{k}}{\beta^*\omega y},\frac{500v}{y^2\omega}\right] \tag{13}$$

The constants in the transport equations for turbulent kinetic energy k and turbulent dissipation ω are obtained from expression $\phi=\phi_1F_1+\phi_2(1-F_1)$. Among them, ϕ_1 is the constant in the Standard $k-\varepsilon$ turbulent model equation and ϕ_2 is the constant in the Standard $k-\omega$ turbulent model equation. The turbulent model constants are as follows: $\beta^*=0.09$, $\alpha_1=5/9$, $\beta_1=0.075$, $\sigma_{k1}=0.85$, $\sigma_{\omega1}=0.5$, $\alpha_2=0.44$, $\beta_2=0.0828$, and $\sigma_{k2}=1$, $\sigma_{\omega2}=0.856$.

2.3. Numerical Calculation Methods

Various discretization methods can be employed to solve the governing equations for viscous flow fields, such as the finite volume, finite element, and spectral methods. Flow field calculation methods encompass the SIMPLE, SIMPLEC, SIMPLER, and PISO algorithms, among others. In this study, the finite volume method was used for spatial discretization. The computational domain was subdivided into a finite number of control volumes, and the governing equations were transformed into algebraic equations through

the discretization process. The convective and diffusive terms are discretized using a second-order upwind scheme and a central difference scheme, respectively. The viscosity flow field was solved using the PISO (Pressure Implicit with Splitting of Operators) algorithm (Issa, 1986) [33]. The PISO algorithm has obvious advantages in solving transient problems. To compute the hydrodynamic performance of the V-type wave dissipation system, it is necessary to capture the free-surface wave height, for which the VOF multiphase flow model proposed by Hirt and Nichols in 1981 [34] was used to track the free surface. The SST $k-\omega$ turbulence model, widely used in engineering applications with high applicability and reliability, was selected for the viscous flow field calculations. The numerical computation process employed unsteady flow to obtain steady-state flow.

3. Three-Dimensional Numerical Wave Tank Calculation Validation

3.1. Model Parameters and Wave Generation Method

A three-dimensional numerical wave tank was established using the velocity inlet wave generation method, with the free surface wave motion model applied at the inlet boundary. By calculating the fluid particle velocity and phase fraction at the boundary, periodic waves were generated. A fifth-order Stokes wave model was used, which can generate wave profiles that are closer to those obtained experimentally compared to lower-order methods. The various parameters of the generated waves, such as free surface position, wave height, water depth, and wavelength, were controlled by setting their values. Additionally, a damping source term was introduced, and a damping dissipation method was applied to set up a dissipation zone at the outlet to eliminate the waves. The fifth-order Stokes wave parameters are shown in Table 1.

Table 1. Wave parameters.

Wave Model	Wave Length	Wave Height	Water Depth	Wave Period
Fifth-order Stokes wave	4 m	0.08 m	2.5 m	1.6 s

The selection of the numerical wave tank computational domain affects the computation time. Considering the subsequent hydrodynamic performance calculation of the V-type wave dissipation system, an appropriate size for the numerical wave tank computational domain was chosen to maintain consistency in domain selection. A three-dimensional numerical wave tank was constructed with dimensions of 20 m in length, 8 m in width, and 4 m in height, with a water depth of 2.5 m and a free surface distance of 1.5 m from the top of the tank. Wave height monitoring points M1 and M2 are set within the numerical wave tank, with M1 and M2 located 1 wavelength and 2.5 wavelengths away from the inlet, corresponding to X = 4 m and X = 10 m, respectively. The arrangement of the wave height monitoring points is shown in Figure 1.

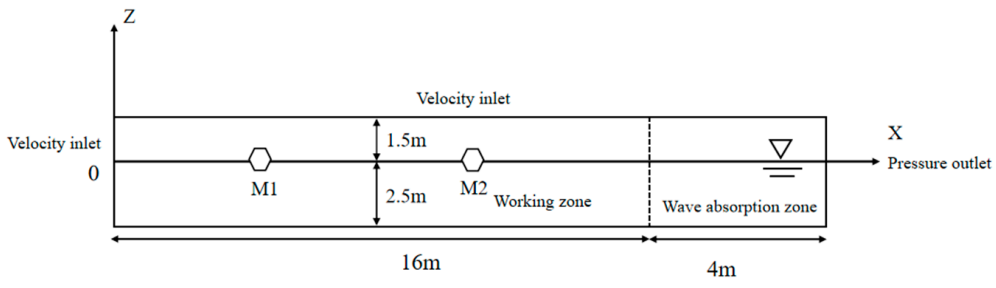
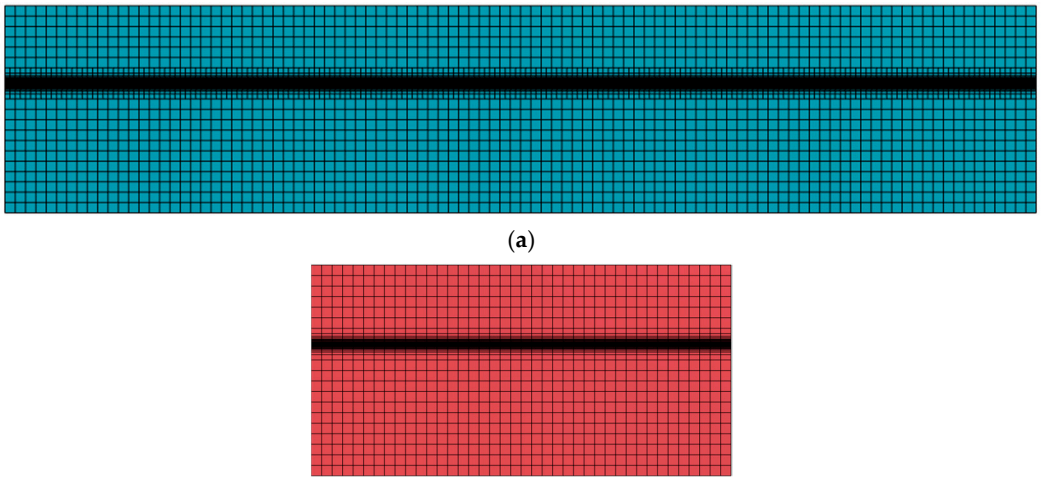


Figure 1. Monitoring point arrangement diagram.

3.2. Grid Division and Boundary Condition Settings

To accurately capture the wave height at the free surface, grid refinement was applied within one wave height above and below the free surface along the *Z*-axis (vertical direction) of the computational domain. Fifteen layers of grid nodes were allocated within this wave height range for the numerical study. In the working section along the *X*-axis (longitudinal direction), the grid was uniformly distributed, and a damping zone with a length of 4 m was established at the downstream end of the domain. The computational domain was discretized using structured grids, with a base grid size of 0.2 m in the X (length), Y (width), and Z (height) directions. Grid refinement was required in the region of wave height variation near the free surface. Based on existing numerical research findings [19], the ratio of the grid spacing in the *Z*-axis (height) direction (Δz) to that in the *X*-axis (length) direction (Δx) near the free surface within one wave height above and below generally should not exceed 1:10. In this study, a ratio of $\Delta z/\Delta x = 1:6$ was adopted. The grid spacing Δz along the height (*Z*-axis) of the computational domain was initially set to 15/A, where A represents the wave height. The grid divisions in the XOY plane and YOZ plane are shown in Figure 2.



(**a**)

(**b**)

Figure 2. Schematic diagram of the grid division in the computational domain: (**a**) schematic diagram of the grid division in the XOY plane; (**b**) schematic diagram of the grid division in the YOZ plane.

The velocity inlet boundary was used for wave generation. Once the initial velocities of the fluid particles at the free surface and below the free surface at the given boundary were specified, wave generation through the velocity inlet was achieved. The fifth-order Stokes wave was selected for the simulation. When the wave height and wavelength of the incident wave are given, the fluid phase fraction and velocity distribution at the inlet can be determined. The inlet face of the numerical wave tank was set as Velocity-inlet, the outlet face was set as Pressure-outlet, the top face was set as Velocity-inlet, the bottom face was set as Wall, and the left and right side faces were set as Symmetry. A three-dimensional isosurface of the wave height and the gas–liquid distribution on the free surface is shown in Figure 3.

3.3. Grid Sensitivity Analysis

The grid resolution significantly affects the quality of numerical wave generation and computational efficiency. To study the impact of grid division methods on numerical wave generation results, a grid sensitivity analysis was conducted. In this study, the number of grid nodes in the wave height range above and below the free surface in the *Z*-axis direction

is taken as the dependent variable. Three grid node configurations are selected within the wave height range, using 10, 15, and 20 layers of grid nodes, while maintaining the ratio of grid spacing in the Z-axis direction (height) to grid spacing in the X-axis direction (length) near the free surface constant, which is $\Delta z/\Delta x = 1:6$. The three sets of computational grid parameters are shown in Table 2. Based on the numerical results, the time–history curves of wave height monitoring points under different grid densities are plotted in Figure 4. In the figure, the black curve represents the theoretical solution (labeled "Theoretical"), the blue curve corresponds to the numerical result with 10 grid layers within the wave height range near the free surface (labeled "10"), the red curve to that with 15 layers (labeled "15"), and the green curve to that with 20 layers (labeled "20").

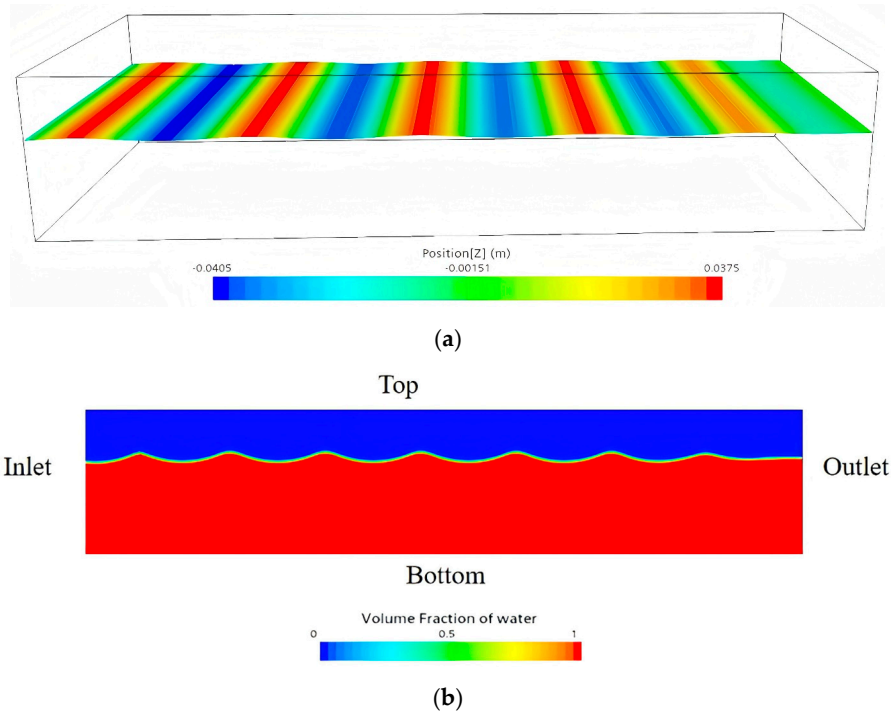


Figure 3. The three−dimensional isosurface of the wave height and the gas–liquid distribution on the free surface: (**a**) three−dimensional isosurface of the wave height; (**b**) gas–liquid distribution on the free surface.

Table 2. Three sets of computational grid parameters.

Grid Conditions	Grid Spacing in the Z Direction	Grid Spacing in the X Direction	Number of Grids
10-layer grid	A/10	6 × A/10	387,000
15-layer grid	A/15	6 × A/15	724,992
20-layer grid	A/20	6 × A/20	1,236,992

As shown in Table 2, the number of grid points with 20 layers in the wave height range near the free surface is approximately 1.7 times that of the 15-layer grid, resulting in a significant decrease in computational efficiency. From the numerical results at wave height monitoring points M1 and M2 in Figure 4, it can be seen that when the number of grid nodes near the free surface increases, wave attenuation is alleviated. Both the 15-layer and 20-layer grids in the wave height range near the free surface meet the computational accuracy requirements. Comparing the three sets of numerical data, it is evident that when a 10-layer grid is used near the free surface, wave attenuation is more significant. The optimization level of the 20-layer grid is similar to that of the 15-layer grid, and

the differences from the theoretical solution are also small. Considering computational efficiency, the 15-layer grid configuration is selected for subsequent computational studies near the free surface wave height range.

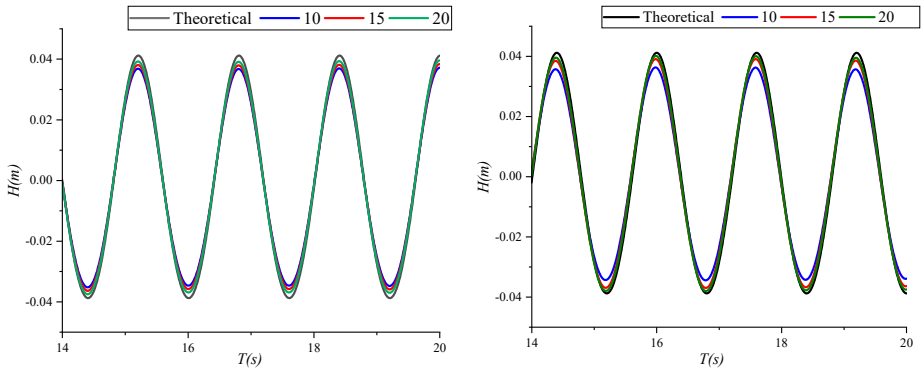


Figure 4. Time–history curves of wave height monitoring points under different grid densities: (**a**) X = 4 m; (**b**) X = 10 m.

3.4. Time Step Sensitivity Analysis

The selection of time step size also affects the accuracy of numerical wave generation. To study the impact of time step size on wave generation results, three different time steps, 0.0025 s, 0.005 s, and 0.01 s, were selected for numerical simulations and comparative analysis under the same grid configuration. Time–history curves of wave height monitoring points under different time steps are shown in Figure 5. In the figure, the black curve represents the theoretical solution (labeled "Theoretical"), the red curve corresponds to the numerical result with a time step of 0.0025 (labeled "0.0025"), the blue curve to that of 0.005 (labeled "0.005"), and the green curve to that of 0.01 (labeled "0.01"). From the numerical results at wave height monitoring points M1 and M2 in Figure 5, it can be observed that as time step decreases, wave numerical accuracy gradually improves, and the results increasingly align with the theoretical values. When the time step is 0.01 s, wave attenuation becomes more significant, and phase deviations are present. The numerical differences at the same wave height monitoring points for time steps of 0.005 s and 0.0025 s are relatively small, with errors within 5% compared to the theoretical values, meeting the wave generation accuracy requirements. To ensure computational efficiency, a time step of 0.005 s was selected for the numerical wave tank and subsequent wave dissipation system calculations.

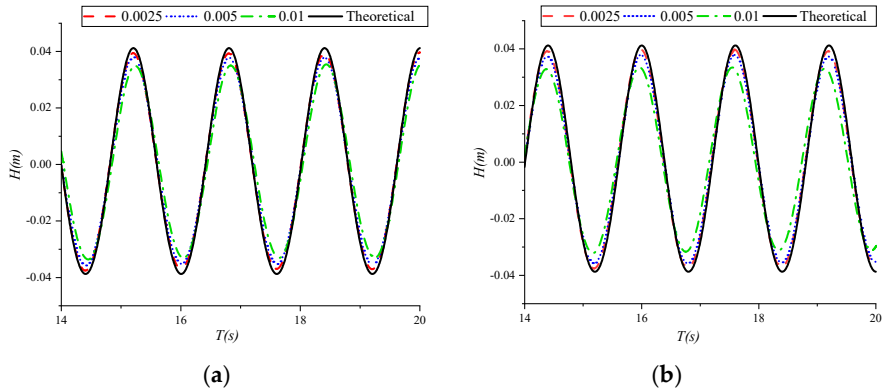


Figure 5. Time−history curves of wave height monitoring points under different time steps: (**a**) X = 4 m; (**b**) X = 10 m.

4. Numerical Wave Tank Wave Dissipation System Validation Study

4.1. Model Parameters

Based on the research of [35], an airbag-type floating breakwater is adopted as the computational model. The structure approximates a cylindrical form with a geometric scale of 1:20, resulting in a model diameter of 0.4 m and a length of 4 m. To ensure sufficient structural rigidity for hydrodynamic assessment, water is injected into the airbag prior to testing. The experiments were performed in a towing tank with the breakwater model positioned transverse to the wave direction under a horizontal mooring arrangement. Two wave gauges (M1 and M2) were deployed along the centerline at distances of 3 m and 5 m downstream of the model to quantify wave attenuation. The prototype conditions represent Sea State 4, characterized by a wave height of 1.5 m and wave periods of 5 s and 6 s. Applying Froude scaling ($\lambda = 20$), since wave behavior is primarily gravity-dominated, the corresponding model-scale wave height is 0.075 m (consistent for both cases), with periods of 1.118 s (Case 1) and 1.342 s (Case 2). The experimental layout is depicted in Figure 6, while the corresponding computational model established using these parameters is presented in Figure 7.

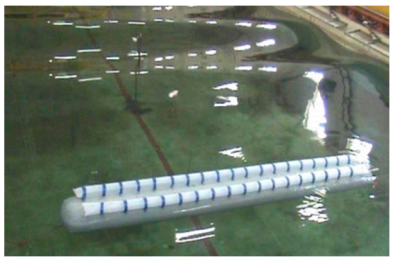


Figure 6. Experimental model.

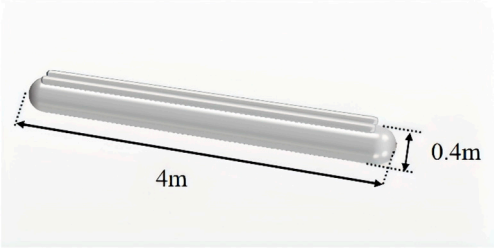


Figure 7. Computational model.

The numerical wave attenuation system adopts identical computational domain selection, boundary condition specifications, and mesh generation techniques as those implemented in the three-dimensional numerical wave tank model. The center of gravity of the floating attenuation device is located 8 m from the velocity inlet boundary, with the model aligned perpendicular to the incident wave direction. Wave monitoring points M1 and M2 are positioned along the central axis at distances of 3 m and 5 m downstream from the leeward side of the structure, respectively. Figure 8 illustrates the overall computational domain configuration of the numerical wave attenuation system.

4.2. Numerical Results Analysis

Numerical simulations of the wave dissipation system in the numerical wave tank were conducted for two different wave conditions, and the variation in wave height elevation at monitoring points M1 and M2 with time is plotted under different operating conditions in Figure 9. In Figure 9, the black curve represents the numerical results for wave height at monitoring point M1 (labeled "M1"), and the red curve represents the numerical results for wave height at monitoring point M2 (labeled "M2"). From

Figure 9, it can be seen that under the same operating condition, the wave amplitude increases as the distance from the wave height monitoring point increases. Additionally, the wave amplitude at the same monitoring point increases with the extension of the period, especially at the M1 wave height point behind the dissipation model, where the effect of period increase on wave amplitude is more significant. When the wave period T is 1.342 s, the wave height differences at M1 and M2 locations gradually decrease with the extension of calculation time.

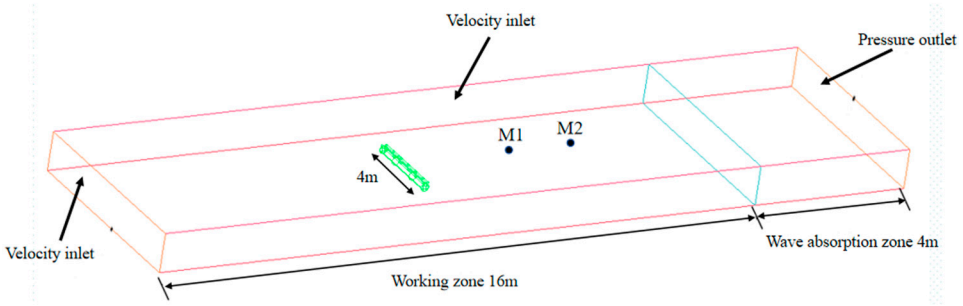


Figure 8. The overall computational domain configuration of the numerical wave attenuation system.

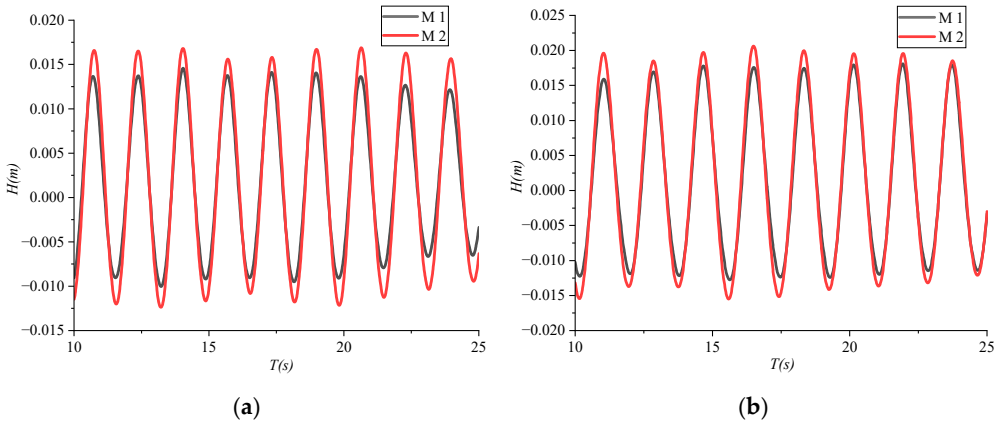


Figure 9. Time history curves of wave height under different operating conditions: (**a**) T = 1.118 s; (**b**) T = 1.342 s.

Numerical results after 20 s under different operating conditions are compared with experimental values. In Figure 10, the red curve represents the numerical results (labeled "Numerical"), and the black dots represent the experimental results (labeled "Experimental"). From Figure 10, it can be seen that the calculated values at wave height monitoring points M1 and M2 under both operating conditions 1 and 2 match well with the experimental values, with small errors. At the M1 wave height monitoring point for both operating conditions, the error between the calculated and experimental values is smaller than that at the M2 wave height monitoring point. This is because M1 is closer to the wave dissipation model than M2, resulting in a shorter time for the waves to reach M1 and less interference. Additionally, compared to operating condition 1, in operating condition 2, the wave height waveform at the M1 and M2 monitoring points shifts backward with increasing computation time. This is due to the increased period and longer calculation time, where the numerical viscous dissipation effect becomes more significant.

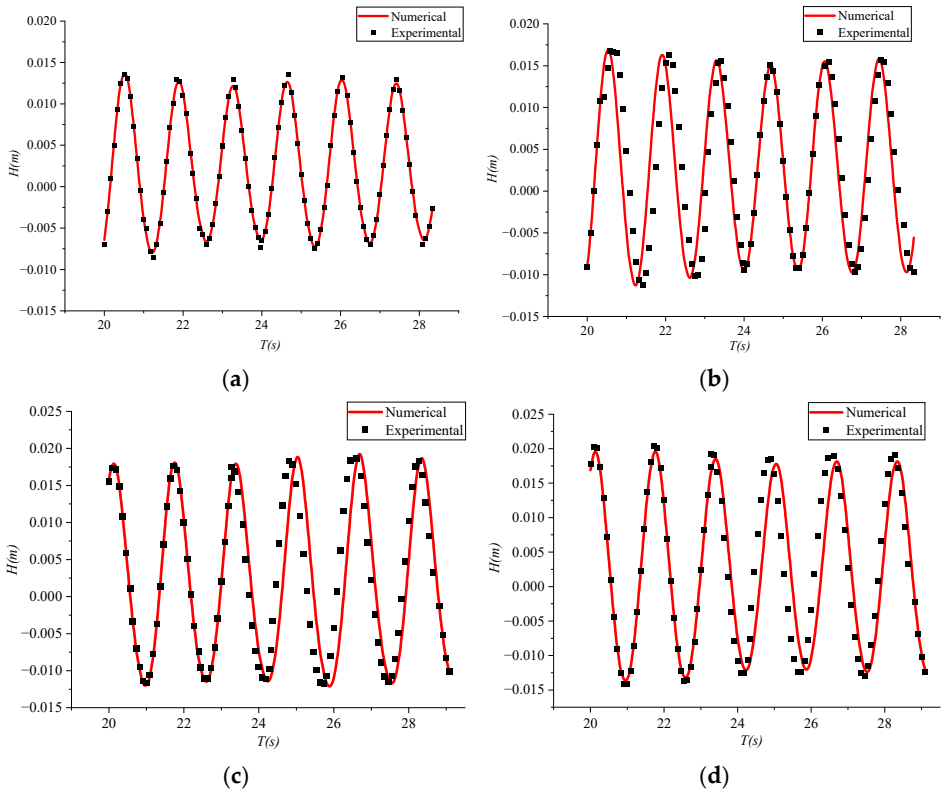


Figure 10. Time history curves of wave height at different locations Drillship: (**a**) operating condition 1 (M1 = 3 m); (**b**) operating condition 1 (M2 = 5 m); (**c**) operating condition 2 (M1 = 3 m); (**d**) operating condition 2 (M2 = 5 m).

Based on the above calculation results, the wave-blocking dissipation effect is analyzed. The wave dissipation performance of the floating dissipator is primarily expressed by the dissipation efficiency δ, and its calculation formula is

$$\delta = \left(1 - \frac{H_t}{H_i}\right) \times 100\% \tag{14}$$

Within the formula, H_t corresponds to the transmitted wave height, while H_i indicates the incident wave height. Based on both numerical and experimental results, the transmitted wave height is taken as the wave height after the oscillation stabilizes. A detailed comparison of the dissipation efficiency results based on numerical and experimental values is shown in Table 3.

Table 3. Comparison of dissipation efficiency results between numerical and experimental values.

Operating Conditions	Monitoring Points	Numerical Value (H_t/m)	Experimental Value (H_t/m)	Numerical Value (δ/%)	Experimental Value (δ/%)
Case 1	M1 (3 m)	0.0247	0.0249	67.07	66.80
	M2 (5 m)	0.0395	0.0400	47.33	46.67
Case 2	M1 (3 m)	0.0424	0.0422	43.47	43.73
	M2 (5 m)	0.0483	0.0491	35.60	34.53

As shown in Table 3, under any given period, the wave dissipation efficiency at M1 (3 m) behind the dissipation model is significantly higher than that at M2 (5 m). When the period T = 1.118 s, the dissipation efficiency at M1 (3 m) is approximately 67%, while at M2 (5 m), the dissipation efficiency is approximately 47%. When the period is extended to T = 1.342 s, the dissipation efficiency at M1 (3 m) decreases to approximately 43%, and at

M2 (5 m), the dissipation efficiency decreases to approximately 35%. The results indicate that as the wave period T increases, the dissipation efficiency shows a significant downward trend, and under the same operating condition, the dissipation efficiency also decreases as the distance from the wave height monitoring point increases.

5. Selection of Optimal Hydrodynamic Performance for Different Configurations of V-Type Wave Dissipation Systems

5.1. Model Parameters

Considering the practical marine landing scenario of launching amphibious landing equipment from a ship's stern hatch, this study investigates the hydrodynamic performance of the V-type wave dissipation system under different configurations. Under normal conditions, a mobile landing platform vessel can conduct equipment and material transfer operations in sea conditions up to Sea State 4 in waters 25 miles (40.2 km) or more from shore. In Sea State 4, the wave height is 1.5 m with a period of 6 s. The original model of the V-type wave dissipation system was selected with a berm width of 8 m, length of 60 m, and water entry depth of 8 m, which meets the operational requirements for coastal wave areas in China's Bohai Sea, Yellow Sea, East China Sea, and South China Sea. The numerical model has a scale ratio of 20. Since wave motion is primarily governed by gravity, the Froude similarity criterion was applied to convert the wave parameters between actual sea conditions and the numerical model experimental conditions, based on the model scale ratio. After conversion, the wave height for the model experiment conditions is 0.075 m, with a period of 1.342 s. The dimensions of the V-type wave dissipation system are shown in Table 4.

Table 4. Dimensions of the V-type wave dissipation system.

Model	Berm Width (m)	Berm Length (m)	Berm Height (m)
Original Model	8 m	60 m	8 m
Numerical Model	0.4 m	3 m	0.4 m

The amphibious landing equipment selected is the publicly available Type 63 light amphibious tank, with a length of 8.435 m, width of 3.2 m, height of 3.122 m, and a combat weight of 18.4 t. To improve computational efficiency, the model is appropriately simplified by treating the amphibious tank as a rectangular prism and neglecting protruding features such as the turret. Using the Froude similarity criterion and maintaining the model scale ratio of 20 for the V-type wave dissipation system, the scale conversion between the original model and the numerical model of the amphibious landing equipment was carried out. The dimensions of the amphibious landing equipment are shown in Table 5.

Table 5. Dimensions of the amphibious landing equipment.

Model	Vehicle Length (m)	Width (m)	Height (m)	Combat Weight (t)
Original Model	8.435 m	3.2 m	3.122 m	18.4 t
Numerical Model	0.42175 m	0.16 m	0.1561 m	0.0023 t

5.2. Layout and Grid Division

A numerical model was established based on the dimensions of the V-type wave dissipation system and amphibious landing equipment. The V-type wave dissipation system consists of an upper airbag and a lower waterbag. The numerical model of a single buoy has a length of 3 m, with a lower waterbag diameter of 0.4 m and an upper airbag diameter of 0.1 m. The layout of the wave dissipation system has a significant impact

on the shielding characteristics of the amphibious landing equipment. Four different layout configurations with angles of 30°, 45°, 60°, and 90° are selected to conduct the computational study of the hydrodynamic characteristics of the V-type wave dissipation system. The models of the V-type wave dissipation system with different layout angles are shown in Figure 11.

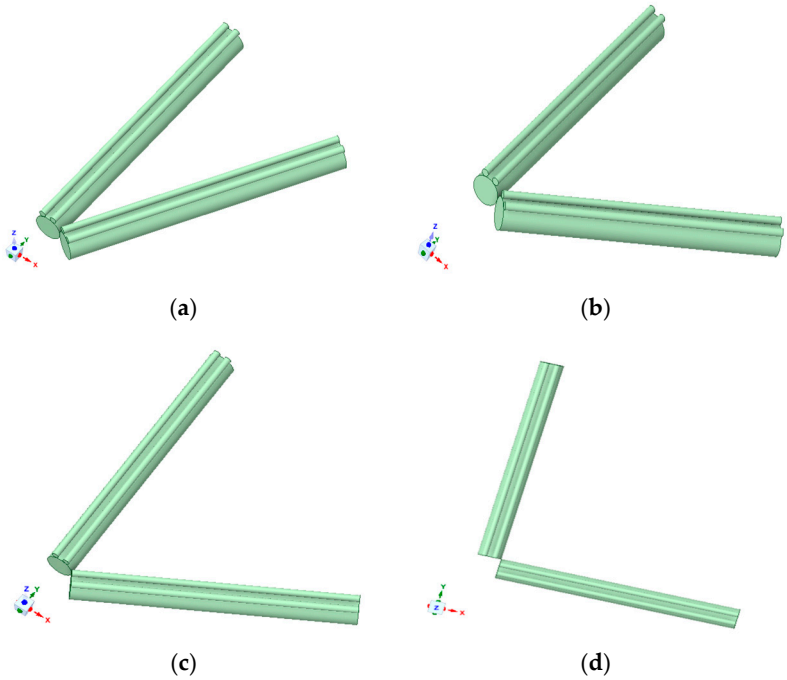


Figure 11. V-type wave dissipation system with different layout angles: (**a**) 30°; (**b**) 45°; (**c**) 60°; (**d**) 90°.

To improve computational accuracy and ensure the grid quality meets application requirements, a hybrid grid division method combining unstructured and structured grids was used. The computational domain is divided into inner and outer domains, with the wave interaction region between the V-type wave dissipation system and amphibious landing equipment being the inner domain, generated using unstructured grids with a basic grid size of 0.005 m. The outer domain of the computational domain uses structured grids, with grid refinement applied within the wave height range of the free surface. The overall computational domain selection, boundary conditions, and outer domain grid division for the V-type wave dissipation system and amphibious landing equipment model are consistent with the settings used for the three-dimensional numerical wave tank model prediction. The grid division of the V-type wave dissipation system and amphibious landing equipment model with a 30° angle is shown in Figure 12.

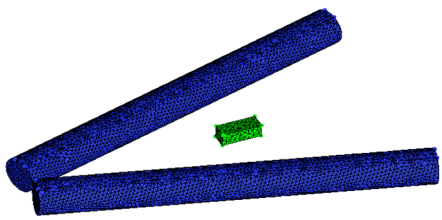


Figure 12. Grid division diagram of the V-type wave dissipation system and amphibious landing equipment model.

To facilitate the comparison of the wave dissipation performance of the V-type wave dissipation system under different layout angles, wave height monitoring points M1 and

M2 were set before and after the V-type wave dissipation system. The wave dissipation effect of the V-type wave dissipation system under different layout angles was analyzed by observing the changes in the amplitude of wave height at monitoring points M1 and M2. The horizontal distances of M1 and M2 from the inlet boundary are X = 4 m and X = 7 m, respectively. P1 is the pressure monitoring point located at the free surface on the bow of the amphibious landing equipment, positioned 8 m from the inlet boundary. The layout of the V-type wave dissipation system monitoring points and a zoomed-in view of the local position are shown in Figure 13.

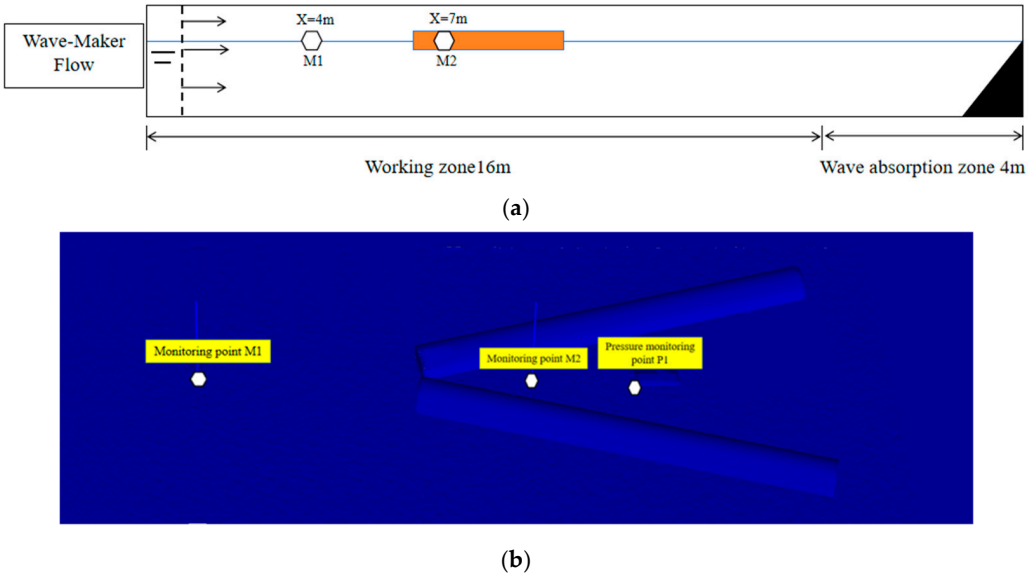


Figure 13. Layout of the V-type wave dissipation system monitoring points and zoomed-in view of the local position: (**a**) monitoring point layout diagram; (**b**) localized enlargement of monitoring point.

5.3. Numerical Results Analysis

Based on the numerical results of the V-type wave dissipation system under four different layout angles, time–history curves of wave height at different monitoring points M1 and M2 are presented in Figure 14. In Figure 14, the black curve represents the numerical results for the 30° layout angle (labeled "30°"), the red curve corresponds to the 45° configuration (labeled "45°"), the blue curve to the 60° arrangement (labeled "60°"), and the green curve to the 90° case (labeled "90°"). From Figure 14, it can be seen that the V-type wave dissipation system's ability to block waves varies with the layout angle. At wave height monitoring point M1, the different layout angles had an insignificant effect on the wave height that had not yet reached the V-type wave dissipation system, with the wave height being close to the theoretical value and showing minimal attenuation. At the downstream monitoring point M2, significant differences in wave height are observed for different layout angles. It is clear that the wave height is smaller for the 30° and 45° layouts and larger for the 60° and 90° layouts. Based on the numerical results from the M1 and M2 wave height monitoring points, the average wave height values at M1 and M2 are selected for wave dissipation effect analysis. The numerical results of the dissipation efficiency for the V-type wave dissipation system under different layout angles are shown in Table 6. In Table 6, δ represents the dissipation efficiency. From Table 6, it can be observed that the V-type wave dissipation system has relatively higher dissipation efficiency for the 30° and 45° layouts, with values of 42.46% and 42.25%, respectively, and the difference between them is small. For the 60° and 90° layouts, the dissipation efficiency is relatively lower. The

wave dissipation effects of the V-type wave dissipation system in different layout angles, from highest to lowest, are as follows: 30°, 45°, 60°, and 90°.

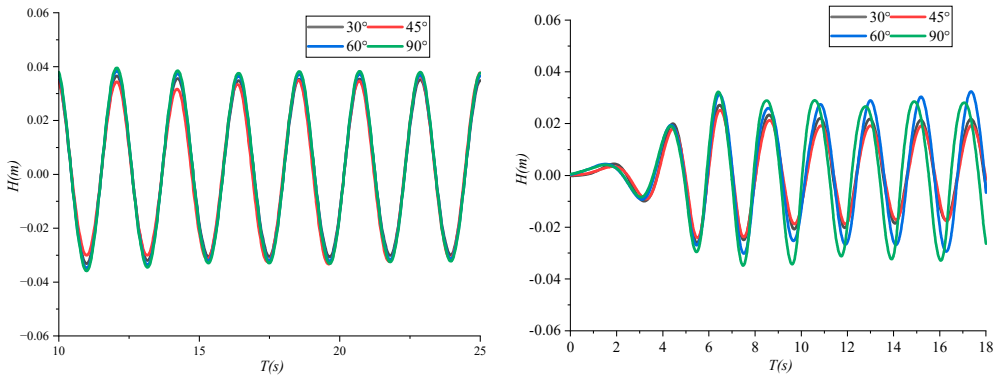


Figure 14. Time−history curves of wave height at monitoring points M1 and M2 under different layout angles: (**a**) monitoring point M1; (**b**) monitoring point M2.

Table 6. Wave dissipation efficiency of the V-type wave dissipation system under different layout angles.

Layout Angles	30°	45°	60°	90°
M1	0.0365 m	0.0355 m	0.0364 m	0.0365 m
M2	0.021 m	0.0205 m	0.028 m	0.030 m
$\delta = (1 - \frac{M2}{M1}) \times 100\%$	42.46%	42.25%	23.07%	17.81%

A comparative analysis was conducted to examine the impact of the V-type wave dissipation system under different layout angles on the hydrodynamic performance of the amphibious landing equipment. Time–history curves of the front-side free surface pressure monitoring point P1 and drag force of the amphibious landing equipment are plotted in Figure 15. In Figure 15, the black curve represents the numerical results for the 30° layout angle (labeled "30°"), the red curve corresponds to the 45° configuration (labeled "45°"), the blue curve to the 60° arrangement (labeled "60°"), and the green curve to the 90° case (labeled "90°"). From Figure 15, it can be seen that the pressure value is smallest under the 45° layout, around 50 N, and largest under the 60° layout, around 250 N, with a gradually increasing trend. As can be seen from Figure 15, the pressure value is the smallest for the 45° configuration, at approximately 50 N, while the largest pressure occurs under the 60° arrangement, reaching about 250 N and showing an increasing trend with prolonged computation time. The pressure values under the 30° and 90° layouts are similar, around 100 N. The overall pressure values, from smallest to largest, are in the order of 45°, 30°, 90°, and 60°. The drag performance curve of the amphibious landing equipment shows that the V-type wave dissipation system under different layout angles has a significant effect on the drag of the equipment. It is evident that the drag is smaller for the 30° and 45° layouts and larger for the 60° and 90° layouts. The drag on the amphibious landing equipment, from smallest to largest, follows the order of 30°, 45°, 90°, and 60°.

Based on the above numerical results, it is evident that the wave dissipation performance of the V-type wave dissipation system varies with different layout angles. Specifically, the 30° and 45° configurations demonstrate more favorable effects on the flow field and the amphibious landing equipment positioned behind the system. The wave dissipation process of the system results from the synergistic effect of multiple mechanisms. The core reason for the difference in wave dissipation performance under different layout angles

lies in their distinct capabilities to perturb the flow field and induce energy transformation. Different layout angles primarily affect the wave dissipation performance by altering the interaction path between waves and the structure. Variations in the layout angle change the effective wave-acting area on the floating body's wave-facing surface, which influences the wave reflection efficiency. Meanwhile, differences in the layout angle lead to more complex diffraction and refraction along the structure, generating a three-dimensional vortex system that enhances turbulent energy dissipation along the wave propagation path. This study comprehensively considers the wave dissipation effect of the V-type wave dissipation system and the drag performance of the amphibious landing equipment. The V-type wave dissipation system under the 30° layout is selected for further research on the hydrodynamic characteristics of the V-type wave dissipation system and amphibious landing equipment under different combined field conditions.

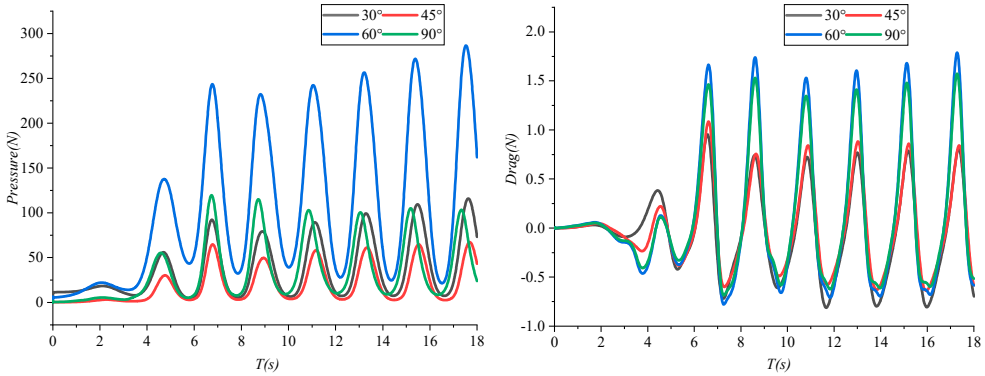


Figure 15. Variation curves of P1 pressure monitoring point and drag of amphibious landing equipment under different layout angles: (**a**) Pressure monitoring point P1; (**b**) Drag of amphibious landing equipment.

6. Numerical Results of the V-Type Wave Dissipation System and Amphibious Landing Equipment Under Different Combined Fields

6.1. Parameters of the Numerical Wave Tank Model Under Different Combined Fields

Based on the numerical results from Section 4, the V-type wave dissipation system under the 30° layout was selected as the computational model to further study the hydrodynamic characteristics of the V-type wave dissipation system and amphibious landing equipment under different combined fields. Separate numerical wave tanks were established for different combined environmental conditions, including a wave-only field, a combined wave-current field, a combined wind-wave field, and a combined wind-wave-current field. The overall computational domain selection and grid division method for the numerical wave tank models remained unchanged. To reduce computational cost, the wind speeds in the coupled wind-wave numerical tank and the coupled wind-wave-current numerical tank were not modeled as gradient winds; instead, a uniform wind speed was applied. The free surface and above are influenced by the wind, which enters vertically and uniformly from the inlet of the numerical tank to establish a homogeneous wind field. A numerical wave tank model for the combined wind-wave-current field is shown in Figure 16.

According to records from the authoritative military reference Jane's Fighting Ships, the design operating capability of similar mobile landing platform vessels typically extends to Sea State 4 to ensure the normal operation of onboard equipment under common meteorological conditions. Therefore, the amphibious landing equipment considered in this study is designed to operate in conditions up to Sea State 4. Based on the parametric

standards for wind, waves, and currents under actual Sea State 4 conditions, the following values were selected: wave height 2 m, wave period 4.95 s, wind speed 6 m/s, and current velocity 0.62 m/s. Based on the model scale ratio of 20, the Froude similarity criterion was applied to convert the parameters between the actual sea conditions and the numerical model experimental conditions. The converted wind-wave-current parameters for the model experiment conditions are shown in Table 7.

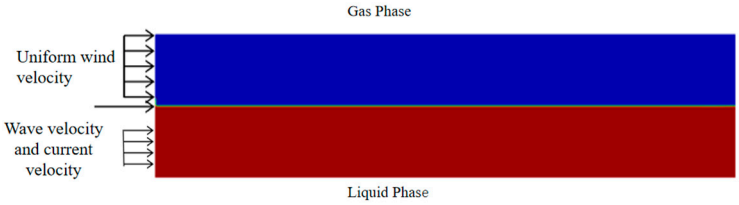


Figure 16. Numerical wave tank for the combined wind-wave-current field grid.

Table 7. Wind-wave current parameters.

Conditions	Model	Wind Velocity	Current Velocity	Wave Height	Test Period (s)
Original sea conditions	20:1	6 m/s	0.62 m/s	2 m	4.95 s
Experimental conditions		1.341 m/s	0.1386 m/s	0.1 m	1.108 s

The positions of the wave height monitoring points for the V-type wave dissipation system under different combined fields are consistent with those in Section 4 and remain unchanged. The horizontal distances of M1 and M2 from the inlet boundary are X = 4 m and X = 7 m, respectively. P1 is the pressure monitoring point at the bow of the amphibious landing equipment at the free surface.

6.2. Analysis of Numerical Results in the Combined Wave-Current Field

To study the effect of current velocity on wave height in combined fields, a combined wave-current field numerical wave tank was established based on the parameters in Table 7. Based on the numerical results from the combined wave-current field and the wave-only field, Figure 17 presents the time–history curves of wave height at monitoring points M1 and M2 under conditions with and without current. In Figure 17, the black curve represents the numerical result from the wave-only field (labeled “wave”), while the red curve corresponds to that from the combined wave-current field (labeled “wave-current”). The figure indicates that the wave heights at monitoring points M1 and M2 in the combined wave-current field show a decreasing trend compared to the results from the wave-only field, and the following current contributes to the reduction in wave height. Additionally, under the influence of the combined wave-current field, the trough wave heights at M1 and M2 exhibit a clear rising trend. This phenomenon indicates that the V-type wave dissipation system demonstrates superior performance under wave-current conditions, where the following current effectively mitigates the wave impact on the system. The wave period also undergoes changes, with the influence of the following current leading to a shorter period. Compared to the time–history curve of wave height in the wave-only field, the corresponding curve in the combined wave-current field exhibits a forward shift phenomenon. The wave period in the combined wave-current field is approximately 1.019 s, which is about 8% shorter than the period in the wave-only field.

Based on the numerical results at wave height monitoring points M1 and M2, the average wave height values at M1 and M2 were selected for wave dissipation effect analysis. The numerical results of the dissipation efficiency of the V-type wave dissipation system

in the wave-only field and combined wave-current field are shown in Table 8. In Table 8, δ represents the dissipation efficiency. From Table 8, it can be seen that the dissipation efficiency of the V-type wave dissipation system is higher in the combined wave-current field compared to the wave-only field. The average wave heights at M1 and M2 in the combined wave-current field are lower than those in the wave-only field, further validating the conclusion drawn from Figure 17 that a following current can reduce wave height.

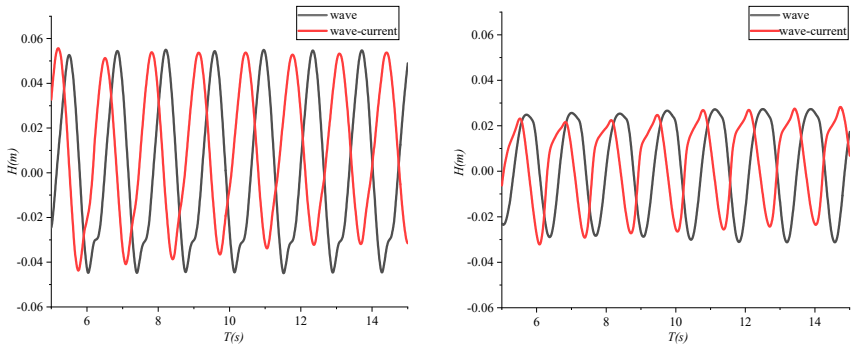


Figure 17. Time−history curves of wave height at monitoring points M1 and M2 with and without current velocity: (**a**) monitoring point M1; (**b**) monitoring point M2.

Table 8. Wave dissipation efficiency of the V-type wave dissipation system in the wave-only field and combined wave-current field.

Conditions	Average Wave Height at M1	Average Wave Height at M2	Dissipation Efficiency δ = (1 − M2/M1)
Wave-only field	0.095 m	0.055 m	42.1%
Combined Wave-current field	0.088 m	0.049 m	44.3%

6.3. Analysis of Numerical Results in the Combined Wind-Wave Field

To study the effect of wind velocity on wave height in combined fields, a combined wind-wave field numerical wave tank was established based on the parameters in Table 7. Based on the numerical results from the combined wind-wave field and the wave-only field, Figure 18 presents the time–history curves of wave height at monitoring points M1 and M2 under conditions with and without wind velocity. In Figure 18, the black curve represents the numerical result from the wave-only field (labeled "wave"), while the red curve corresponds to that from the combined wind-wave field (labeled "wind-wave"). From Figure 18, it can be seen that under the influence of downwind, the numerical results at monitoring points M1 and M2 show a slight increase in wave height compared to the wave-only field, indicating that the wind has a certain excitatory effect on the waves, causing a slight increase in wave height. This is because the wind velocity in the wind field plays a role in supplying energy to the wave field. However, over time, the excitatory effect of wind velocity gradually diminishes, and the wave height difference between the combined wind-wave field and wave-only field decreases. The difference in wave height between monitoring points M1 and M2 before stabilization is significantly larger than that after 14 s when the system stabilizes. This is because, prior to stabilization, the flow field is in a phase where wind velocity influences wave generation, whereas after 14 s, the combined wind-wave field reaches a steady state, with the exchange of momentum and energy approaching equilibrium, leading to stabilized wave conditions in the combined field. Compared to the wave height time–history curve in the wave-only field, the curve the combined wind-wave field exhibits a phase advance phenomenon. However, the overall change in wave period in the combined wind-wave field relative to the wave-only field is

relatively small, which is significantly different from the period variation observed in the combined wave-current field.

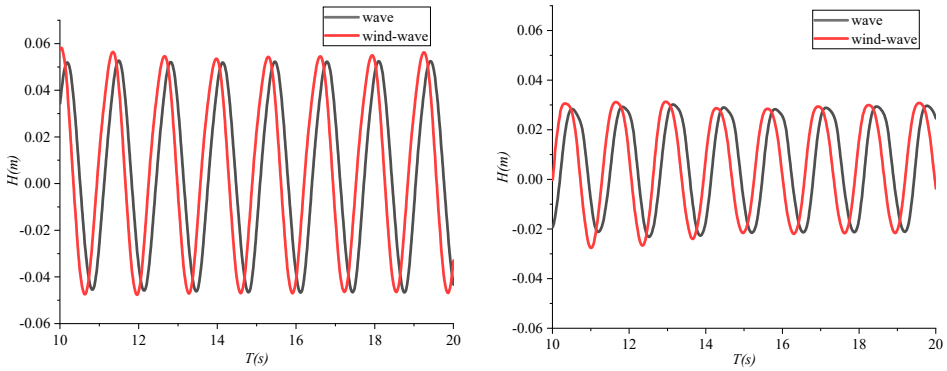


Figure 18. Time−history curves of wave height at monitoring points M1 and M2 under conditions with and without wind velocity: (**a**) monitoring point M1; (**b**) monitoring point M2.

Based on the numerical results at wave height monitoring points M1 and M2, the average wave height values at M1 and M2 were selected for wave dissipation effect analysis. The numerical results of the dissipation efficiency of the V-type wave dissipation system in the wave-only field and combined wind-wave field are shown in Table 9. In Table 9, δ represents the dissipation efficiency. From Table 9, it can be seen that the dissipation efficiency of the V-type wave dissipation system in the combined wind-wave field is lower than in the wave-only field. The average wave height values at M1 and M2 in the combined wind-wave field are greater than the numerical results in the wave-only field, indicating that the V-type wave dissipation system selected in this study performs poorly in blocking wind-waves. This is because the upper structure of the V-type wave dissipation system is relatively low, resulting in a smaller wind blocking area.

Table 9. Wave dissipation efficiency of the V-type wave dissipation system in the wave-only field and combined wind-wave field.

Conditions	Average Wave Height at M1	Average Wave Height at M2	Dissipation Efficiency δ = (1 − M2/M1)
Wave-only Field	0.095 m	0.055 m	42.1%
Combined Wind-Wave Field	0.098 m	0.059 m	39.8%

6.4. Analysis of Numerical Results in the Combined Wind-Wave-Current Field

6.4.1. Wave Height Numerical Results Analysis

With the aim of exploring the combined effects of wind, waves, and current on wave height, a numerical tank for the wind-wave-current combined field was established in accordance with the parameters in Table 7. Based on the numerical results from the combined wind-wave-current field and the wave-only field, Figure 19 presents the time-history curves of wave height at monitoring points M1 and M2 under conditions with and without wind and current. In Figure 19, the black curve represents the numerical result from the wave-only field (labeled "wave"), while the red curve corresponds to that from the combined wind-wave-current field (labeled "wind-wave-current"). Figure 19 indicates that under the action of a following wind-wave-current condition, the wave height at monitoring point M1 shows a certain degree of reduction compared to the wave-only field case, while its peak and trough values exhibit a significant increase. In contrast, the wave height at monitoring point M2 increases substantially relative to the wave-only

field, with its peak and trough values also demonstrating a marked rise compared to the wave-only field conditions. The numerical results indicate that the presence of wind and current exerts a certain excitatory effect on the waves, leading to a noticeable rise. However, the wave height at monitoring point M1 is lower than that under the wave-only field condition. This is attributed to a "stretching" effect induced by the current velocity, which relatively reduces the wave amplitude. The wave height at monitoring point M2 shows no reduction compared to the wave-only field. Analysis indicates that the presence of the V-type wave dissipation system counteracts the wave "stretching" effect induced by the current. Additionally, the relatively low superstructure results in insufficient wave-blocking and sheltering capacity at the upper part of the dissipation system.

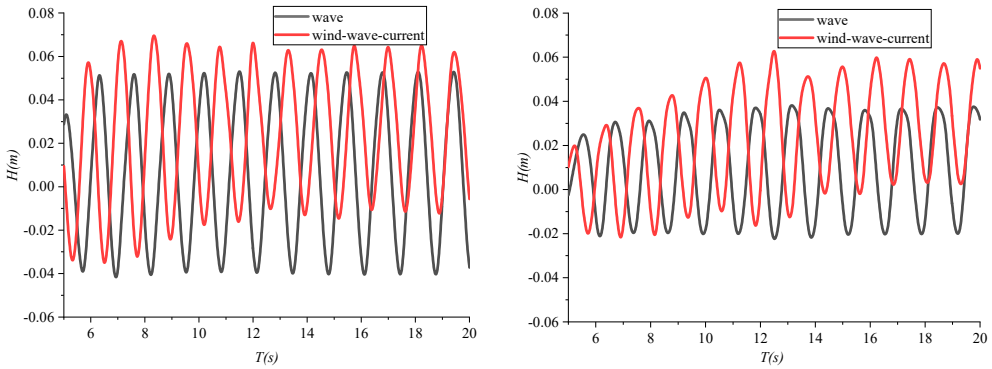


Figure 19. Time−history curves of wave height at monitoring points M1 and M2 under conditions with and without wind and current: (**a**) monitoring point M1; (**b**) monitoring point M2.

Based on the numerical results at wave height monitoring points M1 and M2, the average wave height values at M1 and M2 were selected for wave dissipation effect analysis. The numerical results of the dissipation efficiency of the V-type wave dissipation system in the wave-only field and combined wind-wave-current field are shown in Table 10. In Table 10, δ represents the dissipation efficiency. From Table 10, it can be seen that the dissipation efficiency of the V-type wave dissipation system in the combined wind-wave-current field is much lower than in the wave-only field. This is because the upper structure of the V-type wave dissipation system selected in this study is relatively low. Under the action of wind, waves, and current, the waves exhibit significant upward movement, resulting in insufficient upper sheltering by the dissipation system, thereby reducing its wave dissipation effectiveness.

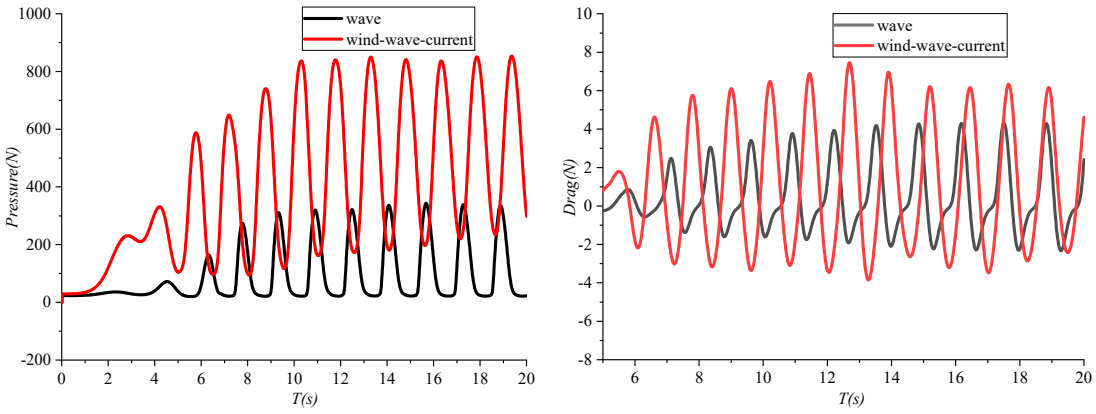
Table 10. Wave dissipation efficiency of the V-type wave dissipation system in the wave-only field and combined wind-wave-current field.

Conditions	Average Wave Height at M1	Average Wave Height at M2	Dissipation Efficiency δ = (1 − M2/M1)
Wave-only field	0.095 m	0.055 m	42.1%
Combined Wind-wave-current field	0.089 m	0.067 m	24.7%

6.4.2. Hydrodynamic Performance Analysis of Amphibious Landing Equipment

A comparative analysis was conducted to examine the impact of the V-type wave dissipation system on the hydrodynamic performance of the amphibious landing equipment in the combined wind-wave-current field and the wave-only field. The time history curves of the front-side free surface pressure monitoring point P1 and drag force of the amphibious landing equipment are plotted in Figure 20. In Figure 20, the black curve

represents the numerical result from the wave-only field (labeled "wave"), while the red curve corresponds to that from the combined wind-wave-current field (labeled "wind-wave-current"). From Figure 20, it can be seen that the slamming pressure at the front of the amphibious landing equipment under the influence of the combined wind-wave-current field is much higher than in the wave-only field. The peak slamming pressure in the combined wind-wave-current field is 800 N, while the peak in the wave-only field is only 300 N. Additionally, the minimum slamming pressure under the combined wind-wave-current field is also significantly higher than in the wave-only field. In the wave-only field, the minimum slamming pressure is approximately 0, which can be considered as no wave action. However, in the combined wind-wave-current field, the minimum slamming pressure increases with time, reaching approximately 150 N, which can be considered as the period without wave action, where the slamming pressure from the combined wind-current effect is 150 N. From the drag performance convergence curve, it can be seen that the drag on the amphibious landing equipment in the combined wind-wave-current field is significantly higher than in the wave-only field. Furthermore, the drag period of the amphibious landing equipment is shorter under the combined wind-wave-current field conditions compared to the wave-only field. This further indicates that the V-type wave dissipation system provides poorer protection against the combined wind-wave-current effect than against the wave-only field, making it more difficult for the amphibious landing equipment to advance under the combined influence of wind, waves, and current.



(**a**) (**b**)

Figure 20. Variation curves of pressure monitoring point P1 and drag of amphibious landing equipment under the combined wind−wave−current field and wave−only field: (**a**) pressure monitoring point P1; (**b**) drag of amphibious landing equipment.

6.5. Comparison and Analysis of Numerical Results for Wave Dissipation Performance Under Different Combined Fields

To further assess the wave dissipation performance and applicable scenarios of the V-type wave dissipation system, a comparative analysis was conducted on the wave heights at monitoring points M1 and M2 under the wave-only field, combined wave-current field, combined wind-wave field, and combined wind-wave-current field. A hierarchical plot of the wave height at monitoring points M1 and M2 under the four conditions is shown in Figure 21. From Figure 21, it can be seen that the wave heights in front and behind the dissipation system differ significantly under the four conditions. Under the combined wind-wave field, the wave height at monitoring point M1 is the highest among the four conditions, followed by the wave-only field. In the combined wind-wave-current field, the wave height at monitoring point M1 ranks as the second lowest among the four conditions, only higher than that in the combined wave-current field. In contrast, the wave height

at monitoring point M2 falls into the high range among the four conditions. This further verifies that the V-type wave dissipation system exhibits relatively poor wave dissipation performance under the combined wind-wave-current field.

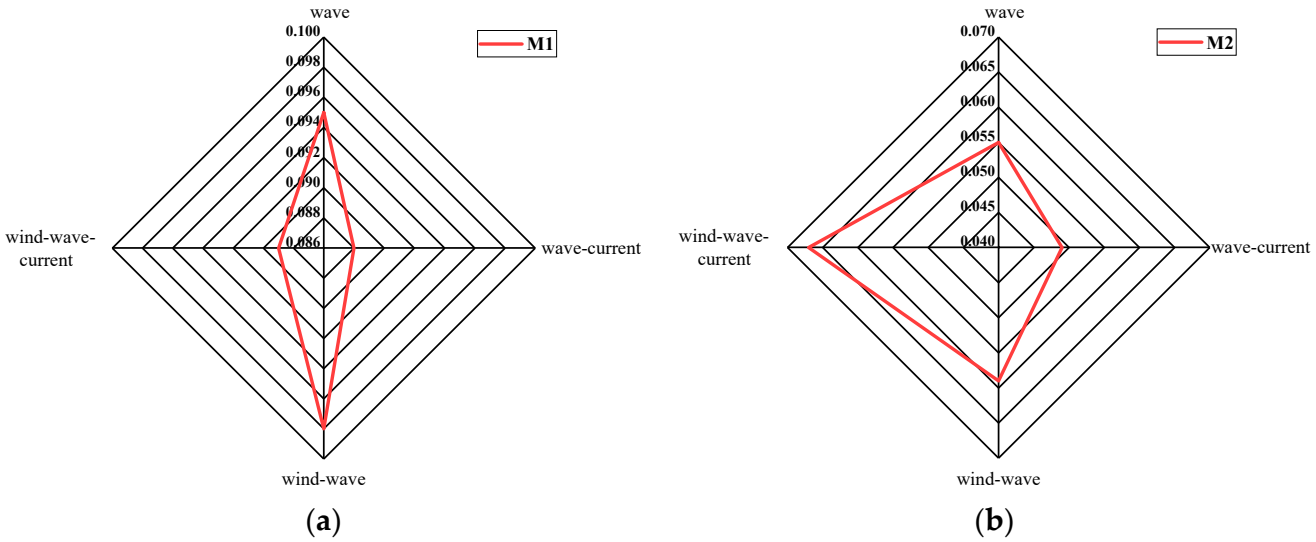
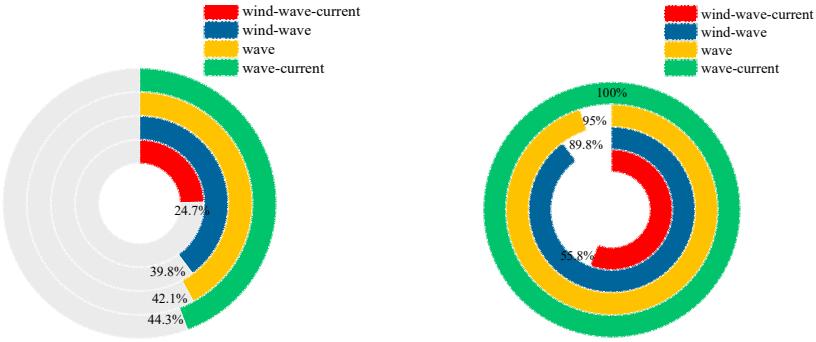


Figure 21. Hierarchical plot of wave height at monitoring points M1 and M2 under four different conditions: (**a**) monitoring point M1; (**b**) monitoring point M2.

Based on the wave height numerical results at monitoring points M1 and M2 under the four conditions, the wave dissipation efficiency of the V-type wave dissipation system and its corresponding proportion under each condition were calculated. The comparison analysis of the dissipation efficiency and its proportion is plotted in Figure 22. From Figure 22, it can be seen that the wave dissipation efficiency is highest under the combined wave-current field, 44.3%, followed by the wave-only field, with a dissipation efficiency of 42.1%. The wave dissipation efficiency is lowest under the combined wind-wave-current field, 24.7%, which is only 55.8% of the dissipation efficiency under the combined wave-current field. To analyze the reasons for the relatively lower wave dissipation efficiency under the combined wind-wave and wind-wave-current conditions, the following factors are considered. The presence of wind transfers momentum to the water surface, leading to continuous wave growth and providing persistent energy input to the waves. This increases the total energy of the incident wave spectrum and enriches its high-frequency components, thereby raising the wave-absorption load on the V-type dissipation system. Especially under wind-wave-current combined conditions, the superposition of the wind-driven current and background current modulates the wave propagation characteristics and intensifies the turbulence in the water body. This may shorten the dissipation path of energy near the V-type dissipation system, allowing for part of the wave energy to propagate more rapidly into the sheltered area. Based on these results, it can be inferred that the V-type wave dissipation system selected in this study is more suitable for the combined wave-current field and wave-only field, with relatively better dissipation performance. For the weaker dissipation capability of the selected V-type wave dissipation system in the combined wind-wave-current field, its dissipation effect can be improved by increasing the height of the upper structure. By raising the height of the upper structure, the system can better resist the impact of wind, waves, and currents on the waves, thereby providing more effective protection.



(**a**) (**b**)

Figure 22. Wave dissipation efficiency and its proportion under four conditions for the V-type wave dissipation system: (**a**) wave dissipation efficiency; (**b**) proportion of wave dissipation efficiency.

7. Analysis and Discussion

Based on the numerical results of this paper, the following analysis and discussion is presented. First, regarding the verification of the wave dissipation system in the numerical wave tank, an airbag-type floating breakwater was employed for computational validation. During the model tests, water was injected into the airbag to provide a certain degree of rigidity. In the numerical simulation, the floating breakwater was treated as a rigid body by default. The small discrepancies between the numerical results and experimental data verify the accuracy and reliability of the numerical method adopted in this study. However, the hydrodynamic validation model only involves a standalone floating breakwater, without considering the multi-body coupled motion response between the dissipation system and other structures. As a result, the complexity of the flow field and the nonlinearity of the motions were not fully validated, indicating certain limitations in the present approach.

Secondly, given that the amphibious landing equipment model was appropriately simplified, this simplification influenced the prediction of its resistance performance and the motion response associated with wave-structure interaction. The geometric discrepancies in hull form design resulting from model simplification, along with the associated differences in wetted surface area, introduced uncertainties into the accurate prediction of form resistance and frictional resistance for the amphibious landing equipment, thereby leading to computational errors. Furthermore, this study did not account for the prediction of motion response, which represents a limitation. Nevertheless, the prediction methodology employed in this paper can still provide a valuable reference for the engineering application of amphibious landing equipment.

Furthermore, calculations based on the wave-current combined field and the wind-wave combined field indicate the following: Compared to the wave-only field, the wave height results under the wave-current combined field show a decreasing trend, and the wave-height time histories exhibit a forward-shift phenomenon. A following current can reduce the wave height and shorten the wave period, a numerical conclusion that has been corroborated in the literature [36]. In contrast to the wave-only field, the wave height results under the wind-wave combined field display a certain increase. A following wind also causes a forward shift in the wave-height time histories, but its effect on the wave period is relatively minor. The literature [37,38] provides strong theoretical and numerical support for these conclusions.

Finally, numerical results based on the combined wind-wave-current interaction show that, compared to the wave-only field, the wave height at monitoring point M1 under the wind-wave-current combined field decreased slightly, while the wave height at monitoring

point M2 increased substantially. Both the crest and trough values at M1 and M2 exhibit a significant increase. Under the wind-wave-current combined condition, the resistance of the amphibious landing equipment is notably higher than that in the wave-only field, and the resistance period is shorter. Among the four different combined fields, the wave dissipation efficiency of the V-type dissipation system is the lowest under the wind-wave-current combined field, making forward advancement of the amphibious landing equipment more difficult when subjected to the combined action of wind, waves, and current. To improve the hydrodynamic performance of the V-type dissipation system under wind-wave-current conditions, increasing the height of its upper structure could be considered to better mitigate the influence of wind-wave-current interactions on the waves, thereby enhancing its wave dissipation effectiveness.

8. Conclusions

This study numerically investigates the hydrodynamic characteristics of the V-type wave dissipation system and amphibious landing equipment under different combined fields using CFD methods. The following key conclusions are drawn:

(1) A three-dimensional numerical wave tank was constructed, and the numerical results were validated against theoretical values. Using grid sensitivity and time step sensitivity analyses, it is found that the number of grid points in the free surface range significantly affects the accuracy of numerical wave generation. Setting 15 layers of grids within the wave height range provides high computational efficiency and accuracy. A time step of 0.005 s or 0.0025 s yields high numerical wave-generation precision.

(2) The hydrodynamic characteristics of the V-type wave dissipation system under four different layout angles were studied under wave-only field conditions. The results show that the wave dissipation efficiency of the V-type system is relatively high for the 30° and 45° arrangements, reaching 42.46% and 42.25%, respectively. Combined with the hydrodynamic characteristics of the amphibious landing equipment, these configurations prove to be more favorable for the flow field and the amphibious landing equipment positioned behind.

(3) Wave-dissipation performance and applicable scenarios of the V-type wave dissipation system arranged at the 30° angle under four different combined fields were evaluated numerically. The results indicate that the highest wave dissipation efficiency, 44.3%, is achieved under the wave-current combined field, followed by 42.1% under the wave-only field. The efficiency is lowest under the wind-wave-current combined field at 24.7%. Based on the present study, the selected V-type dissipation system is more suitable for wave-current combined and wave-only conditions, providing a valuable reference for its engineering application.

Author Contributions: Conceptualization, J.H. and C.S., methodology J.H., C.S. and J.D., software C.S. and X.Y., validation J.D., formal analysis C.S. and X.Y., investigation J.D., resources D.Z., data curation X.Y. and D.Z., writing—original draft preparation J.H., writing—review and editing D.Z., visualization X.Y., supervision J.D., Project administration J.H. and J.D., funding acquisition J.H., X.Y. and D.Z. All authors have read and agreed to the published version of the manuscript.

Funding: This research was funded by the National Natural Science Foundation of China (Grant Nos., 52401380 and 52301321), and the Natural Science Foundation of Jiangsu Province of China (Grant Nos., BK20220652 and BK20251030).

Data Availability Statement: The original contributions presented in this study are included in the article. Further inquiries can be directed to the corresponding author.

Conflicts of Interest: The authors declare no conflicts of interest.

References

1. Han, L.A.; Xi, Y.Y. *Port Hydraulic Engineering Structures*; China Communications Press: Beijing, China, 2010.
2. Wang, Y.X.; Wang, G.Y. Research Progress and Engineering Applications of Nearshore Floating Breakwater Structures. *Shipbuild. China* **2002**, *43*, 314–321.
3. Zhou, L.; Chen, K.; Zhai, S.; Niu, Z.; Hu, M. Experimental Study of the Effects of Different Floating Breakwater on Wave Absorbing. *Adv. Struct. Eng.* **2014**, *16*, 1683–1700.
4. Ji, C.Y.; Bian, X.Q.; Hou, F.L.; Guo, J.T.; Lian, Z.X.; Yuan, Z.M. Experimental study on hydrodynamic characteristics of a new type floating breakwater with opening pass and wing structure. *Ocean. Eng.* **2022**, *259*, 111923. [CrossRef]
5. Koraim, A.S.; Rageh, O.S. Effect of under connected plates on the hydrodynamic efficiency of the floating breakwater. *China Ocean. Eng.* **2014**, *28*, 349–362. [CrossRef]
6. Loukogeorgaki, E.; Yagci, O.; Kabdasli, M.S. 3D Experimental investigation of the structural response and the effectiveness of a moored floating breakwater with flexibly connector modules. *Ocean. Eng.* **2014**, *91*, 164–180.
7. He, F.; Li, J.D.; Pan, J.P.; Yuan, Z.M. An experimental study of a rectangular floating breakwater with vertical plates as wave-dissipating components. *Appl. Ocean. Res.* **2023**, *133*, 103497. [CrossRef]
8. Wang, G.Y.; Ren, B.; Wang, Y.X. Experimental study on hydrodynamic performance of arc plate breakwater. *Ocean. Eng.* **2016**, *111*, 593–601. [CrossRef]
9. Wang, F.J. *Computational Fluid Dynamics Analysis: Principles and Applications of CFD Software*; Tsinghua University Press: Beijing, China, 2004.
10. Finnegan, W.; Goggins, J. Numerical simulation of linear water waves and wave-structure interaction. *Ocean. Eng.* **2012**, *43*, 23–31. [CrossRef]
11. Li, Y.; Lin, M. Regular and irregular wave impacts on floating body. *Ocean. Eng.* **2012**, *42*, 93–101. [CrossRef]
12. Peng, J.; Liu, Y.; Liu, J.; Li, Y. Research of Numerical Wave Generation and Wave Absorption Simulation Based on Momentum Source Method. *Int. J. Digit. Content Technol. Its Appl.* **2013**, *121*, 66–76.
13. Chen, Y.L.; Hsiao, S.C. Generation of 3D water waves using mass source wavemaker applied to Navier–Stokes model. *Coast. Eng.* **2016**, *109*, 76–95. [CrossRef]
14. Prasad, D.D.; Ahmed, M.R.; Lee, Y.H.; Sharma, R.N. Validation of a piston type wave-maker using Numerical Wave Tank. *Ocean. Eng.* **2017**, *131*, 57–67. [CrossRef]
15. Zhang, X.S.; Ma, S.; Duan, W.Y. A new L type floating breakwater derived from vortex dissipation simulation. *Ocean. Eng.* **2018**, *164*, 455–464. [CrossRef]
16. Christensen, E.D.; Bingham, H.B.; Friis, A.P.S.; Larsen, A.K.; Jensen, K.L. An experimental and numerical study of floating breakwaters. *Coast. Eng.* **2018**, *137*, 43–58. [CrossRef]
17. Li, X.Y.; Wang, Q.; You, Z.J.; Guo, W.J.; Zhang, Z.B.; Zhan, C.; Zhang, Z.C.; Wang, L.X.; Li, Q. Wave attenuation performance and the influencing factors of a lower arc-plate breakwater. *China Ocean. Eng.* **2020**, *34*, 89–98. [CrossRef]
18. Abdullah, S.F.; Fitriadhy, A. Application of genetic algorithm for optimum hydrodynamic performance of twin pontoon floating breakwater. *J. Waterw. Port Coast. Ocean. Eng.* **2020**, *146*, 04019040. [CrossRef]
19. Zhang, C.; Magee, A.R. Effectiveness of floating breakwater in special configurations for protecting nearshore infrastructures. *J. Mar. Sci. Eng.* **2021**, *9*, 785. [CrossRef]
20. Ran, X.L.; Wang, B.; Duan, W.J.; Chen, K.; Gan, J. Study on Wave Attenuation Performance of V-shaped Flexible Floating Breakwater. *J. Wuhan Univ. Technol. (Transp. Sci. Eng.)* **2021**, *45*, 76–81.
21. Sun, B.; Zhang, H.J.; Yang, S.L.; Yang, L.; Chen, S.Z.; Li, C. The hydraulic characteristics and shape optimisation of submerged Box-type floating breakwater. *Ships Offshore Struct.* **2022**, *17*, 2329–2339. [CrossRef]
22. Yuan, P.Y.; Zhao, Y.; Zhang, X.Y. Study on the Nonlinear Wave Climbing Characteristics of Floating Breakwaters in a Numerical Water Tank. *Shipbuild. China* **2023**, *64*, 134–142.
23. Ji, C.Y.; Bian, X.Q.; Xu, S.; Guo, J.T.; Huo, F. Numerical study on the hydrodynamic performance of floating breakwaters with complex configurations. *Ocean. Eng.* **2023**, *273*, 114032. [CrossRef]
24. Cartwright, B.; Renilson, G.; Macfarlane, G.; McGuckin, D.; Esi, A.P.; Cannon, S. Motions of a landing craft in a flooded well dock-effect of well dock design. In Proceedings of the International Conference on Military Support Ships, Sydney, Australia, 3–5 October 2007.
25. Yoon, S.-H.; Seo, K.-H. Well Dock Design and Assessment of Relative Motions During the Operation of the Landing Crafts Within Well Dock. *J. Soc. Nav. Archit. Korea* **2012**, *49*, 164–173. [CrossRef]
26. Hu, X.Q. *Hydrodynamic Performance Analysis of Ships with Hold Compartments*; Jiangsu University of Science and Technology: Zhenjiang, China, 2019.

27. Ji, C.Y.; Yong, C.; Ke, Y.; Gaidai, O. Numerical and experimental investigation of hydrodynamic performance of a cylindrical dual pontoon-net floating breakwater. *Coast. Eng.* **2017**, *129*, 1–16. [CrossRef]
28. Chorin, A.J. A numerical method for solving incompressible viscous flow problems. *J. Comput. Phys.* **1967**, *2*, 12–26. [CrossRef]
29. Versteeg, H.K.; Malalasekera, W. *An Introduction to Computation Fluid Dynamics: The Finite Volume Method*; Wigley: New York, NY, USA, 1995.
30. Menrer, F.R.; Kuntz, M.; Langtry, R. Ten years of industrial experience with the SST turbulence model. *Turbul. Heat Mass Transf.* **2003**, *4*, 35–42.
31. Wilcos, D.C. Multi Scale Model for Turbulence Flows. In Proceedings of the AIAA 24th Aeropace Sciences Meeting, Reno, NV, USA, 6–9 January 1986; American Institute of Aeronautics and Astronautics: Reston, VA, USA, 1986.
32. Hu, J.M.; Li, T.L.; Lin, Y.; Guan, G.; Zheng, Z.B. Prediction of ship power and speed performance based on RANS method. *Int. Shipbuild. Prog.* **2017**, *64*, 51–78. [CrossRef]
33. Issa, R.I. Solution of the implicitly discretised fluid flow equations by operator-splitting. *J. Comput. Phys.* **1986**, *62*, 40–65. [CrossRef]
34. Hirt, C.W.; Nichols, B.D. Volume of fluid (VOF) method for the dynamics of free boundary. *J. Comput. Phys.* **1981**, *39*, 201–225. [CrossRef]
35. Su, L.; Lin, X.R.; Wang, X.G. Numerical simulation of airbag type floating breakwater on wave blocking and wave elimination. *Port Waterw. Eng.* **2021**, *8*, 1–7.
36. Ke, S.T.; Wang, S.; Zhang, W.; Wang, Y.; Wang, T.G. Comparative analysis on wave propagation and evolution mechanism under the coupling effect of wind, wave and current fields. *J. Harbin Eng. Univ.* **2021**, *42*, 9.
37. Wang, K.; Wan, Y.C.; Liu, T.H.; Fan, T.H.; Mai, Z.H.; Wu, H. Study on the joint distribution of wind and wave in offshore wind farms of Guangdong sea area. *Shipbuild. China* **2022**, *6*, 273–284.
38. Chen, Y.Q.; Chen, A.R.; Ma, R.J. A joint probabilistic model of design wave and wind parameters for offshore structures under typhoon circumstances. *J. Highw. Transp. Res. Dev.* **2016**, *33*, 89–94.

Disclaimer/Publisher's Note: The statements, opinions and data contained in all publications are solely those of the individual author(s) and contributor(s) and not of MDPI and/or the editor(s). MDPI and/or the editor(s) disclaim responsibility for any injury to people or property resulting from any ideas, methods, instructions or products referred to in the content.